JOURNAL OF GEOPHYSICAL RESEARCH: SOLID EARTH, VOL. 118, 689–697, doi:10.1029/2012JB009358, 2013

Geodetic slip rates in the southern San Andreas Fault system: Effects of elastic heterogeneity and fault geometry

E. O. Lindsey[1] and Y. Fialko[1]

Received 2 April 2012; revised 14 November 2012; accepted 16 November 2012; published 4 February 2013.

[1] We use high resolution interferometric synthetic aperture radar and GPS measurements of crustal motion across the southern San Andreas Fault system to investigate the effects of elastic heterogeneity and fault geometry on inferred slip rates and locking depths. Geodetically measured strain rates are asymmetric with respect to the mapped traces of both the southern San Andreas and San Jacinto faults. Two possibilities have been proposed to explain this observation: large contrasts in crustal rigidity across the faults, or an alternate fault geometry such as a dipping San Andreas fault or a blind segment of the San Jacinto Fault. We evaluate these possibilities using a two-dimensional elastic model accounting for heterogeneous structure computed from the Southern California Earthquake Center crustal velocity model CVM-H 6.3. The results demonstrate that moderate variations in elastic properties of the crust do not produce a significant strain rate asymmetry and have only a minor effect on the inferred slip rates. However, we find that small changes in the location of faults at depth can strongly impact the results. Our preferred model includes a San Andreas Fault dipping northeast at 60°, and two active branches of the San Jacinto fault zone. In this case, we infer nearly equal slip rates of 18 ± 1 and 19 ± 2 mm/yr for the San Andreas and San Jacinto fault zones, respectively. These values are in good agreement with geologic measurements representing average slip rates over the last 10^4–10^6 years, implying steady long-term motion on these faults.

Citation: Lindsey, E. O., and Y. Fialko (2013), Geodetic slip rates in the southern San Andreas Fault system: Effects of elastic heterogeneity and fault geometry, *J. Geophys. Res. Solid Earth*, *118*, 689–697, doi:10.1029/2012JB009358.

1. Introduction

[2] The southern San Andreas Fault system contains a number of seismically active faults that pose a significant earthquake hazard to nearby densely populated areas. One measure of seismic hazard is the rate of strain accumulation in the brittle upper crust. Geodetic observations have shown that a total of 35–40 mm/yr of dextral motion is accommodated across the San Andreas Fault (SAF), San Jacinto Fault (SJF), and Elsinore Fault (EF) in Southern California [*Johnson et al*., 1994; *Bennett et al*., 1996]. This motion is primarily accommodated by earthquakes on the respective faults, making an understanding of the pattern of strain accumulation a critical task for evaluation of seismic hazard in the area.

[3] The details of slip partitioning between the major faults of the Southern SAF system remain a subject of debate. Geologic measurements of slip rates on timescales of 10^4–10^6 years suggest rates of 14–19 mm/yr on the SAF [*Van der Woerd et al*., 2006; *Behr et al*., 2010] and 11–20 mm/yr on the SJF [*Rockwell et al*., 1990; *Blisniuk et al*., 2010; *Kendrick et al*., 2002; *Janecke et al*., 2010]. In comparison, most geodetic studies have suggested a somewhat higher slip rate of 21–25 mm/yr on the SAF [*Meade and Hager*, 2005; *Fay and Humphreys*, 2005; *Becker et al*., 2005; *Fialko*, 2006; *Spinler et al*., 2010]. *Platt and Becker* [2010] reported approximately equal rates of 14 mm/yr on the two faults with additional slip on other minor faults, while *Lundgren et al*. [2009] have proposed that the SJF is faster than the SAF, with a slip rate of up to 24 mm/yr. Further complicating the problem is the observation that for both faults the maximum strain rates are systematically offset to the east of the geologically mapped fault traces [*Fialko*, 2006].

[4] Variability in the reported slip rate estimates in part reflects the nonuniqueness and trade-offs inherent in inversions of geodetic data. Confidence intervals provide a formal measure of the uncertainty in these estimates, reflecting the effect of measurement errors and other sources of noise. However, estimates of slip rates on the SAF and SJF have low formal uncertainties relative to the large differences between independent estimates [see, e.g., *Lundgren et al*., 2009, Table 1]. These disagreements must therefore result from the use of different data, or from different assumptions in the forward models used to interpret these data, resulting in a bias that is not reported in the formal confidence intervals. Differences in forward models may include rheology (elastic

All Supporting Information may be found in the online version of this article.

[1]Institute of Geophysics and Planetary Physics, Scripps Institution of Oceanography, University of California San Diego, La Jolla, California, USA.

Corresponding author: E. O. Lindsey, Institute of Geophysics and Planetary Physics, Scripps Institution of Oceanography, University of California San Diego, La Jolla, California, USA. (elindsey@ucsd.edu)

2169-9313/13/2012JB009358

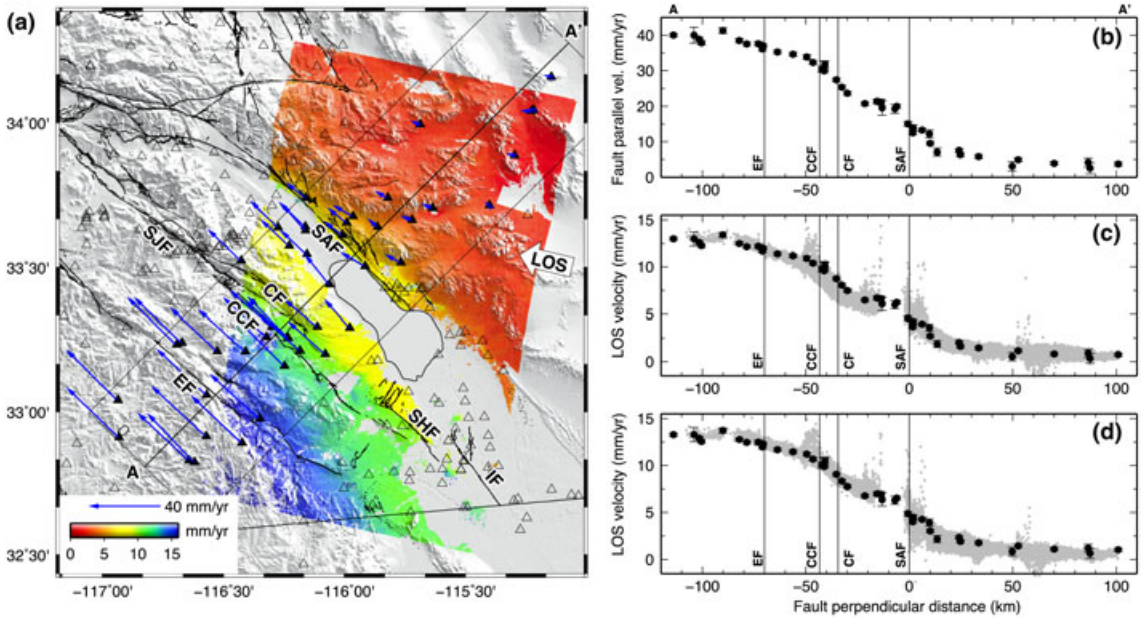

Figure 1. (a) Map of study region showing horizontal GPS velocities in the North America Fixed frame [*Shen et al*., 2011; T. Herring, personal commun., 2011] and InSAR data from ERS-1/2 Track 356 [*Manzo et al*., 2011]. Faults are from USGS quaternary fault map (available http://earthquakes.usgs.gov/regional/qfaults/, accessed September 2011), with labels: Coyote Creek Fault (CCF), Clark Fault (CF), Elsinore Fault (EF), Imperial Fault (IF), San Andreas Fault (SAF), Superstition Hills Fault (SHF), and northern San Jacinto Fault (SJF). (b) Horizontal GPS velocities projected onto fault-parallel direction. (c) InSAR LOS velocities and horizontal GPS velocities projected onto the radar look direction, illustrating systematic disagreement in the western part of the profile. (d) InSAR LOS and projected GPS velocities after applying remove-restore correction to ensure agreement between the data sets at long wavelengths.

or viscoelastic), model domain (two-dimensional (2D) or three-dimensional (3D)), material properties (homogeneous, layered or heterogeneous medium), and the assumed fault geometry at depth.

[5] Of these factors, model rheology has received the most consideration. Purely elastic models consider a fault locked to some depth D, below which slip occurs uniformly on a deep extension of the fault plane [*Savage and Burford*, 1973]. This conceptually simple model requires only two parameters, but has nonetheless proven quite successful in matching observed deformation patterns. An alternative model assumes that below the elastic upper crust, plate motion is accommodated by a comparatively broad viscoelastic flow [*Nur and Mavko*, 1974; *Savage and Prescott*, 1978]. Previous studies have demonstrated that elastic and viscoelastic models cannot be distinguished on the basis of fit to geodetic data alone [*Savage*, 1990; *Fay and Humphreys*, 2005]. Furthermore, models employing laboratory-derived constitutive laws indicate that substantial strain localization may be expected beneath mature transform faults even in a purely viscous regime [e.g., *Takeuchi and Fialko*, 2012], so that differences between dislocation and viscoelastic models may primarily reflect simplifying assumptions in both classes of models, rather than different deformation scenarios.

[6] In this study, our focus is on the possible bias introduced by assumptions about material heterogeneity and fault geometry, both of which have been proposed as causes of the observed asymmetry in strain rate across the major faults of the Southern SAF system [*Fialko*, 2006; *Lundgren et al*., 2009]. We therefore restrict our attention to models using screw dislocations in a 2D elastic medium with arbitrary variations in elastic properties.

2. Data and Methods

2.1. Geodetic Data

[7] To constrain our models, we use a combination of regional GPS velocities and interferometric synthetic aperture radar (InSAR) line-of-sight (LOS) observations from ERS-1/2 Track 356. The GPS data are a combination of continuous and campaign velocities from the Crustal Motion Model 4 (CMM4) data set [*Shen et al*., 2011] and additional continuous sites operated by the UNAVCO Plate Boundary Observatory network. Using the program velrot, the two sets were rotated into the North America fixed reference frame (T. Herring, personal commun., 2011). The updated data include several new sites in the Coachella Valley that lend further support to observations of a significant asymmetry in the strain rate across the southern SAF, with a higher strain rate to the east of the fault trace [*Fialko*, 2006; *Lundgren et al*., 2009; *Fay and Humphreys*, 2005] (Figures 1a and 1b).

[8] The InSAR data set includes 141 interferograms spanning the period 1992–2007 [*Manzo et al*., 2011], nearly doubling the time span of data used previously in studies of this region [*Fialko*, 2006; *Lundgren et al*., 2009]. The LOS velocities were estimated using a small-baseline algorithm with several continuous GPS stations in the region used to remove orbital errors; for further details see *Manzo et al*. [2011].

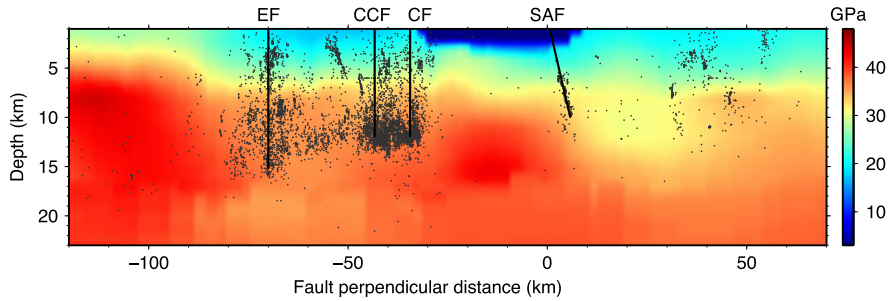

Figure 2. Shear modulus computed from the SCEC regional velocity model CVM-H 6.3 [*Suess and Shaw*, 2003; *Plesch et al*., 2009], with relocated seismicity (black dots) [*Lin et al*., 2007] and geometry of locked faults in our preferred model (black lines).

Although the GPS coverage is quite dense across much of the region, the InSAR is needed to accurately resolve the strain rate in areas where the GPS coverage is low, or GPS solutions are affected by local site effects.

[9] We selected data within a 60 km wide, 250 km long profile oriented perpendicular to the faults and centered on the SAF trace at 33.55°N (Figure 1a). The location of the profile was chosen to satisfy the assumption of 2D antiplane deformation as closely as possible. In particular, the profile excludes areas whose motion may be contaminated by slip transfer to the eastern California shear zone to the north, and to the Imperial Fault to the south. Within the selected profile, deviations from fault-parallel motion are small, and primarily occur close to the SAF where a slight compressional component is visible across the fault. Several stations near the southern end of the SAF and the Coachella canal showed a significant (greater than 3 mm/yr) non-strike-slip component of motion, possibly due to local hydrological effects or a transfer of slip to the Imperial Fault, and were therefore excluded from our data set (open symbols in Figure 1a).

[10] The remaining 46 GPS velocities (see Table S1 in the auxiliary material) are shown projected onto the fault azimuth at N46°W in Figure 1b, and projected onto the radar look direction in Figure 1c for comparison with the InSAR.[1] When plotting the InSAR velocities, we adjust for the variation in radar incidence angle to present a more straightforward comparison with the LOS-projected GPS velocities. This is done by multiplying each pixel by $\sin(\bar{\delta})/\sin(\delta)$, where δ is the incidence angle, which varies across the track and with topography, and $\bar{\delta} = 23.3°$ is the mean value. In our inverse models, the predicted velocities are compared directly to the fault-parallel velocities measured with GPS, and to the satellite LOS velocities using actual incidence angles at each pixel.

[11] The improved accuracy of both the horizontal GPS and InSAR LOS velocities compared to earlier results reveals a systematic difference between the two data sets, which cannot be attributed to orbital artifacts. While good agreement is observed across the eastern half of the profile and at the western edge, LOS-projected GPS velocities are systematically higher than the InSAR LOS velocities in the Santa Rosa Mountains, just west of the Coachella Valley (Figure 1c). Although the disagreement of 1–2 mm/yr in the LOS direction is small, it amounts to a difference of up to 5 mm/yr if interpreted as motion in the fault-parallel direction.

[12] One possible cause of the disagreement is a secular vertical uplift in the area, which would decrease the radar LOS velocities without affecting the horizontal GPS values. When the vertical components are included in the projection of GPS velocities onto the radar look direction, the results are more consistent with the InSAR. This suggests that the InSAR LOS velocities contain both the strike-slip deformation we wish to interpret and a small amount of uplift that is not accounted for by our model. To ensure agreement between the data sets and exclude any vertical motion from the InSAR LOS velocities, we adopted a remove-restore method proposed by *Wei et al*. [2010], which relies on the more accurate horizontal GPS velocities to constrain the long wavelength characteristics of the LOS velocity field. We remove an interpolated map of the horizontal GPS velocities from the InSAR data set, high-pass filter the residual at 70 km wavelength, and add the result back to the GPS velocity map. This procedure ensures that the InSAR velocities agree with the GPS at the longest wavelengths, while preserving the short-wavelength features that make the InSAR contribution valuable in the near field of major faults in our study area. The corrected data set is shown in Figure 1d.

2.2. Elastic Structure of the Crust

[13] We use the Southern California Earthquake Center (SCEC) Community Velocity Model CVM-H 6.3 [*Suess and Shaw*, 2003; *Plesch et al*., 2009] to constrain variations in the elastic properties of the crust along our profile and evaluate the effect of these variations on the surface deformation pattern. Estimated seismic velocities and densities from this model are used to compute the shear modulus on a uniform 1 km grid along our profile extending to 50 km depth. Because the pattern of deformation resulting from material heterogeneities depends only on variations in the shear modulus and not its absolute value, we are not concerned with the possible frequency dependence of elastic moduli [e.g., *O'Connell and Budiansky*, 1974; *Cleary*, 1978].

[14] The shear wave velocities reported by the SCEC model are extremely low in the top 1–2 km of the Salton trough, owing to the presence of uncompacted sediments. We imposed a minimum shear modulus of 3 GPa in this region to improve convergence of our numerical models and prevent spurious errors. The sediments are underlain by a high rigidity mafic lower crust, as shown in Figure 2. The net effect of this rigidity structure on the surface deformation

is complex; the soft upper and rigid lower layers compete to respectively increase or decrease the strain rate in this area. *Fialko* [2006] suggested that a rigid lower crust could potentially explain the observed asymmetry in the geodetic profile across the SAF, but the required increase in shear modulus across the fault (a factor of two to five) appears to be too high in comparison to the values inferred from tomography, which suggest a ratio of only ~1.3. *Fay and Humphreys* [2005] modeled the Salton trough as a one-dimensional layered structure embedded in a layered half space, and found that the effect of weak sediment near the surface was more significant than that of the strong lower crust, but the net effect was minimal and degraded the overall fit to the geodetic data.

[15] We computed surface displacements in the heterogeneous domain shown in Figure 2 using the method of *Barbot et al*. [2009], which accounts for arbitrary variations in material properties by introducing an equivalent distribution of fictitious body forces. The computation is implemented in a parallel finite-difference framework with nonuniform grid size. We computed the elastic Green's function for dislocations representing each fault at a range of locking depths. The deformation arising from any desired combination of slip rates and locking depths on the three faults is then obtained by superposition. This reduces the number of computationally expensive solutions to the problem to a few hundred, and forward models may then be computed without any added cost relative to the homogeneous case. To ensure consistent accuracy between dislocations at different locking depths, we maintain the grid size at 15 points per locking depth within 10 locking depths of the fault both laterally and vertically, with the total domain extending 100 locking depths from the fault in all directions.

2.3. Constraints on Fault Geometry

[16] The second potential source of bias we examine is the assumed fault (or dislocation) geometry. In elastic models, the position of the dislocation edge below the locked fault defines the inflection point in the surface velocity and the maximum surface strain rate. Therefore, an alternative explanation for the observed asymmetric strain rate across the SAF is that the fault may be dipping to the northeast in the Coachella Valley, which would offset the dislocation edge at depth by 5–10 km, depending on the locking depth [*Fialko*, 2006]. This hypothesis stemmed from the location of microseismicity in the region, which is offset to the east of the SAF trace (Figure 2) [*Lin et al*., 2007]. The small amount of transpression observed in GPS velocities near the fault (Figure 1a) is also consistent with the proposed fault dip, as are earthquake focal mechanisms [*Lin et al*., 2007]. In addition, the dipping seismicity pattern is aligned with a contrast in the elastic moduli at midcrustal depth (Figure 2). *Fuis et al*. [2012] suggested a similar dipping geometry of the southern SAF based on seismic velocity anomalies extending into the upper mantle. Note that in an elastic medium, the deformation pattern arising from a semi-infinite dislocation is controlled only by the position of the dislocation edge, not the dip of the dislocation itself [e.g., *Segall*, 2010].

[17] In the southern San Jacinto fault zone, slip at the surface is partitioned between the Clark Fault (CF) and Coyote Creek Fault (CCF) branches [*Petersen and Wesnousky*, 1994; *Blisniuk et al*., 2010]. The localized surface expression of the CF terminates at the southern end of the Santa Rosa Mountains, and only the CCF has a continuously mapped trace in the San Felipe Hills area west of the Salton Sea (Figure 1a). As a result, most geodetic models have assumed that the CCF is the only active strand of the southern SJF [e.g., *Bennett et al*., 1996; *Meade and Hager*, 2005; *Fay and Humphreys*, 2005; *Spinler et al*., 2010; *Loveless and Meade*, 2011]. However, the observation of an asymmetric strain profile across that strand [*Fialko*, 2006], along with a continuing lineament of seismicity to the south of the CF [*Lin et al*., 2007], suggests that the CCF may not be the main active branch of the San Jacinto Fault at depth. *Fialko* [2006] suggested an alternative geometry that includes localized deformation below both the CCF and the southern continuation of the CF. This model is more consistent with geologic evidence indicating that the CF has accumulated substantially more slip than the CCF over its lifetime [*Sharp*, 1967; *Blisniuk et al*., 2010] and recent mapping indicating that the CF does not terminate at the southern end of its mapped trace, but continues southeast as a series of distributed folds and smaller faults through the San Felipe Hills [*Janecke et al*., 2010].

[18] Below, we present inversions for fault slip rates and locking depths for a range of model assumptions: vertical or dipping SAF, and simple (CCF branch only) or complex (CF and CCF branches) geometry of the SJF. The results indicate that fault geometry has a significant impact on the inferred model parameters, even when the assumed lateral position of the dislocation edge varies by as little as a few kilometers.

2.4. Inverse Method

[19] For each model, we use a Bayesian Monte Carlo method to find the best-fitting fault parameters as well as their uncertainties. We chose a Markov chain method known as slice sampling [*Neal*, 2003], which generates a set of samples distributed in parameter space according to the model probability distribution function (pdf), $P(\mathbf{m})$. The algorithm is described below for a univariate distribution where the model depends on a single parameter x; the full multivariate distribution is sampled by updating each parameter in turn repeatedly.

[20] For a parameter x, slice sampling operates as follows: begin at some point x_0 and compute the forward model $\mathbf{m}[x_0]$. The model probability is then $p_0 = P(\mathbf{m}[x_0])$, apart from an unknown normalization constant. Choose a random value p' from a uniform distribution between 0 and p_0. The next value x_1 is then chosen uniformly from the x axis, with choices being rejected until $p_1 = P(\mathbf{m}[x_1]) > p'$. The effect is that uniformly distributed samples are generated within the area under a curve proportional to the model pdf, so that for a large number of steps the distribution of samples along x is also proportional to the pdf (see *Neal* [2003] for further details). A large number of independent walks with random starting points may be combined to ensure the model is not stuck in a single local maximum of the pdf. This algorithm is similar to Gibbs sampling, but with the advantage that neither an analytic form of the pdf nor the normalization constant need be known in advance, resulting in a more general algorithm and a significant computational cost savings [*MacKay*, 2003].

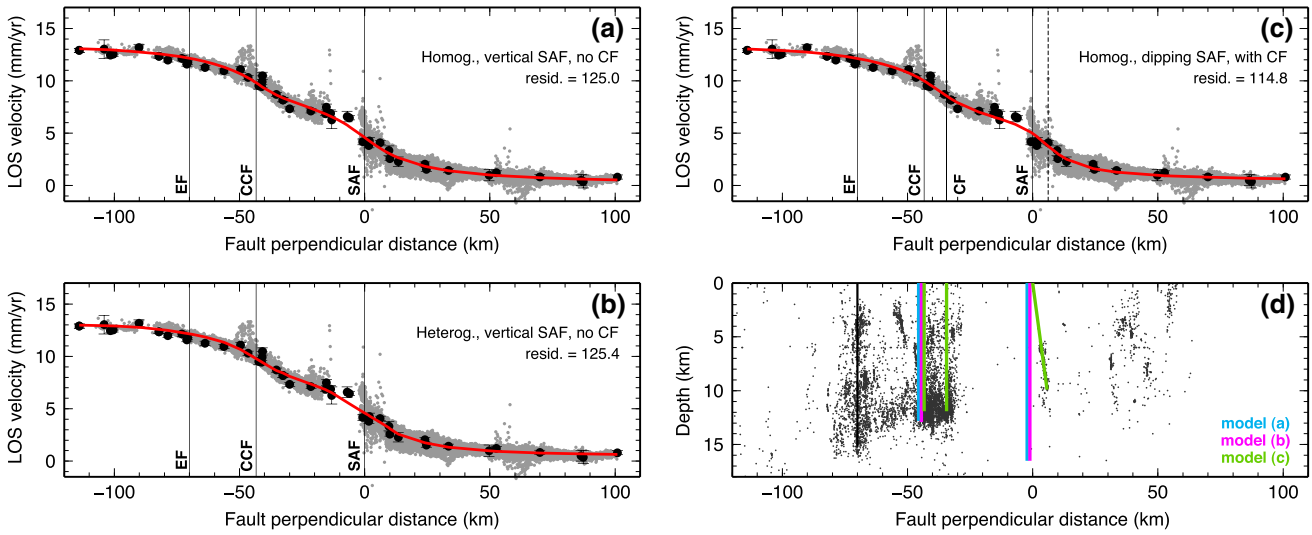

Figure 3. Best fitting model predictions compared to the geodetic data: (a) Simple geometry, homogeneous domain. (b) Simple geometry, heterogeneous domain. (c) Proposed fault geometry includes an active CF and dipping SAF; dashed line indicates the horizontal position of the SAF dislocation edge. The fit is slightly improved in the region between the CF and SAF. (d) Inferred locking depths compared to seismicity [*Lin et al.*, 2007]. EF is fixed at 15 km locking depth and 3 mm/yr slip rate in all models.

[21] In our case, we assume uncorrelated Gaussian error statistics for the geodetic data and define the probability distribution function as

$$P(\mathbf{m}) = A \exp\left(\frac{1}{2}\ (\mathbf{m}-\mathbf{d})^T \mathbf{C}^{-1} (\mathbf{m}-\mathbf{d})\right), \qquad (1)$$

where **m** and **d** are vectors representing the modeled and observed deformation at points along the profile. A is a normalization constant that does not affect the sampling procedure. **C** is the data covariance matrix, assumed to be diagonal. To avoid overfitting some continuous GPS sites with extremely low reported measurement uncertainties (0.1 mm/yr or less), we imposed a minimum uncertainty of 0.5 mm/yr in the inversion. For the InSAR data, the appropriate uncertainties are not readily available. Based on preliminary inversions treating the GPS and InSAR data independently, we found the noise level to be comparable to the GPS and therefore set the relative weighting factor so that the two data sets contribute equally to the misfit value [e.g., *Fialko*, 2004].

[22] To accelerate the forward modeling step in the case of a heterogeneous structure, we precomputed the elastic Green's functions for each fault at each locking depth, simplifying the forward model computation to a linear combination of these solutions. In this case, a set of several thousand samples accurately representing the five-dimensional pdf can be collected in a few minutes on a single CPU. For a higher dimensional model, the number of samples required increases approximately linearly with the number of parameters.

3. Results

[23] The basic model consists of a 2D homogeneous elastic half space with three parallel faults extending vertically below their mapped surface traces: the SAF, CCF, and the EF. The Elsinore Fault is located at the edge of our profile and is associated with a relatively small amount of strain, making its slip rate and locking depth difficult to constrain in an inversion. Thus, for simplicity we fixed the slip rate and locking depth of the EF at 3 mm/yr and 15 km respectively, based on geologic estimates and the depth of seismicity in the region [*Petersen and Wesnousky*, 1994; *Lin et al.*, 2007].

[24] The best-fitting pattern of deformation for the case of simple fault geometry is shown in Figure 3a. The inferred slip rates are 25 ± 1 mm/yr and 13 ± 1 mm/yr for the SAF and CCF, respectively, with locking depths of 16 ± 2 km and 10 ± 3 km. These values are similar to those reported by other studies using a homogeneous elastic domain with the same fault geometry, including 3D block models [*Meade and Hager*, 2005; *Becker et al.*, 2005; *Spinler et al.*, 2010; *Loveless and Meade*, 2011]. The similarity of these results suggests that the choice of 2D or 3D domain is not an important factor in estimating slip rates at the location of our profile, as intended.

3.1. Elastic Structure

[25] For the heterogeneous half-space, the best fitting model is shown in Figure 3b. There is virtually no change in the locking depth for either fault, but there is a slight (2 mm/yr) decrease in the slip rate of the SAF, with no corresponding increase in the CCF rate (Table 1). We verified that this is not an artifact of the numerical model, but rather due to the layered nature of the heterogeneous structure. The vertical variation in shear modulus is significantly stronger than the lateral variation (Figure 2); this causes the surface deformation anomaly to become narrower compared to the prediction for the homogeneous half-space [*Savage*, 1998; *Fialko et al.*, 2001]. If the geodetic data do not extend sufficiently far from the fault, this introduces a trade-off between the inferred slip rate and the heterogeneous structure, which can account for the reduced total slip rate. Aside from this effect, the heterogeneous and homogeneous models are nearly indistinguishable, suggesting that material heterogeneity in this region does not introduce a significant strain asymmetry or cause a noticeable bias in the results.

Table 1. Comparison of Results for Each Set of Model Assumptions Considered in the Text

Domain	SJF	SAF	SAF velocity (mm/yr)	SAF depth (km)	SJF velocity (mm/yr)	SJF depth (km)	Weighted Residual
Homog.	CCF	vert.	25.0 ± 1.5	16.2 ± 1.9	12.9 ± 1.4	10.4 ± 2.8	125.0
Heterog.	CCF	vert.	22.9 ± 1.2	16.5 ± 1.8	12.8 ± 1.2	10.8 ± 2.6	125.4
Homog.	CCF	**dip**	$\mathbf{19.2 \pm 0.9}$	$\mathbf{9.2 \pm 1.0}$	$\mathbf{18.5 \pm 1.4}$	$\mathbf{14.4 \pm 2.5}$	150.4
Heterog.	CCF	**dip**	$\mathbf{18.3 \pm 0.8}$	$\mathbf{10.0 \pm 1.0}$	$\mathbf{17.6 \pm 1.1}$	$\mathbf{15.2 \pm 2.5}$	143.7
Homog.	CCF, CF	vert.	24.2 ± 1.6	16.5 ± 1.9	13.0 ± 1.5	8.7 ± 2.7	117.0
Heterog.	CCF, CF	vert.	22.2 ± 1.3	16.4 ± 1.9	12.7 ± 1.2	8.6 ± 2.4	119.2
Homog.	CCF, CF	**dip**	$\mathbf{18.0 \pm 1.1}$	$\mathbf{9.9 \pm 1.2}$	$\mathbf{18.7 \pm 1.6}$	$\mathbf{11.9 \pm 2.9}$	114.8
Heterog.	CCF, CF	**dip**	$\mathbf{17.4 \pm 1.0}$	$\mathbf{10.6 \pm 1.1}$	$\mathbf{17.4 \pm 1.3}$	$\mathbf{11.9 \pm 2.8}$	113.9

3.2. Fault Geometry

[26] When the SAF is allowed to dip at 60° with the other parameters held constant, the inferred model parameters change significantly (Table 1). The inferred SAF slip rate drops to 18 ± 1 mm/yr, transferring 6 mm/yr to the SJF. The SAF locking depth is reduced to 10 ± 1 km, in better agreement with the observed distribution of seismicity in the area (Figure 3d). The slip rate is in much better agreement with geologic rates reported for the SAF at Biskra Palms [*Van der Woerd et al.*, 2006; *Behr et al.*, 2010]. On the other hand, the slip rate on the CCF strand of the SJF (19 ± 1 mm/yr) is higher than most studies have reported previously. Because the slip rate is correlated with the locking depth, the CCF locking depth increases to 14 km, resulting in a lower near-fault strain rate that degrades the model fit to the data.

[27] If the San Jacinto Fault zone is modeled as two dislocations below the CCF and CF traces at equal depth, the net SJF slip is divided between the two faults, widening the region undergoing deformation at depth, and shifting the location of highest strain rate to the east of the CCF. Due to the proximity of the two fault strands, the tradeoff in slip rate between them is nearly perfect, so it is not possible to resolve which branch carries more slip. In our model, we fixed the CCF at 8 mm/yr and allowed the CF slip rate to vary as a parameter in the inversion, while forcing the locking depth of the two strands to be equal. In this way, the total number of parameters in the inversion is kept constant. If we change the assumed slip rate of the CCF, or instead fix the CF and allow the CCF to vary, the net slip rate remains identical within the uncertainty. Thus, although there is little constraint on the slip rate of either fault, we can confidently infer the net slip rate accommodated by the SJF zone, and this value is reported in Table 1. The result is a moderately improved fit to the data, although the net slip rate does not change significantly compared to the simpler three-fault case.

[28] Our preferred model includes both a dipping SAF and two active SJF strands; the best fitting model velocities are shown in Figure 3c; the result has the best overall fit to the geodetic data (Table 1) and reproduces much of the observed strain rate asymmetry on both fault zones, although the GPS data in the Coachella Valley suggest an even flatter velocity profile than the model can produce. The inferred slip rates are similar to the model with a dipping SAF only, but the locking depth of the SJF branches is 12 km, in better agreement with the depth distribution of seismicity (Figure 3d). Partitioning the higher SJF slip rate of 19 ± 2 mm/yr onto two branches also renders a better agreement with geologic data; observations of CCF offsets suggest that the long-term fault slip rate is only 2–5 mm/yr [*Petersen and Wesnousky*, 1994; *Janecke et al.*, 2010], while the CF appears to accommodate most of the total SJF offset.

[29] In each of our models, the SJF and SAF slip rates trade off strongly with each other, with a correlation of −0.8 to −0.85. The correlation between slip rate and locking depth for each fault is also high, limiting the precision with which we can infer either value independently. The 2D marginal

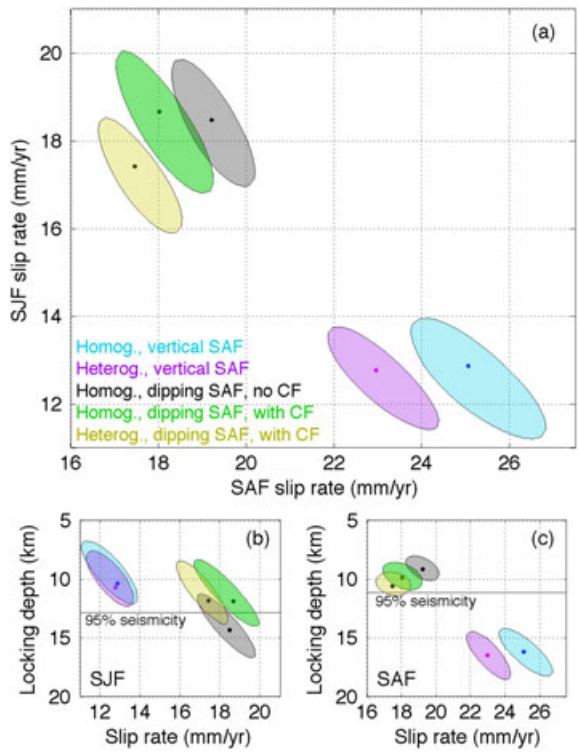

Figure 4. (a) Best fitting model parameters and 1 σ Bayesian confidence regions showing tradeoff between SAF and SJF slip rate for five sets of model assumptions considered in the text. (blue) Homogeneous half-space with a simple three-vertical-fault geometry; (purple) same fault geometry but considering the effects of heterogeneous elastic properties; (gray) homogeneous model with a dipping SAF; (green) homogeneous model with preferred fault geometry: both a dipping SAF and two active SJF branches, the CCF and CF; (yellow) preferred fault geometry with heterogeneous material properties. (b, c) Tradeoff between fault slip rate and locking depth for SJF and SAF, respectively. Line indicates depth above which 95% of seismicity has occurred.

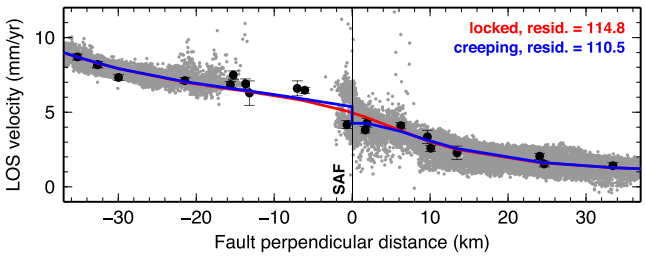

Figure 5. Best fitting modeled and observed geodetic velocities near the SAF, showing the effect of including 2.7 mm/yr creep on the upper 3 km of the dipping SAF. The effect is visible only in the near field (<5 km), and slightly improves the model fit to the data.

probabilities (Figure 4) indicate the range of acceptable models under each set of assumptions, and further highlight the observation that the effect of the assumed fault geometry on the model parameters can be much larger than is suggested by the formal uncertainty reported for a single model.

3.3. Effect of Surface Creep

[30] Parts of the Coachella section of the SAF are associated with surface creep of 2–4 mm/yr, which may be episodically triggered by nearby large earthquakes [*Sieh and Williams*, 1990; *Rymer*, 2000; *Rymer et al*., 2002; *Wei et al*., 2011]. The signature of shallow creep is visible in the InSAR data set in the near field of the fault trace (Figure 1), but the creep rate and depth are difficult to constrain from these data alone because of the lack of coherent radar pixels in the Coachella Valley, and because subsidence of the valley due to agricultural activity may contaminate the LOS signal. We considered a model in which the rate and depth extent of shallow creep are included as parameters in the inversion, and found that the best fitting value of the creep rate is 2.5–3 mm/yr, although there is virtually no constraint on its depth extent (Figure S1). A depth of 3 km is most consistent with the depth of sediment inferred from seismic data [*Lovely et al*., 2006]; this depth has been shown to be a good predictor of creep depth on the nearby Superstition Hills Fault [*Wei et al*., 2009].

[31] Figure 5 shows a modeled creep of 2.7 mm/yr on the dipping fault plane extending to 3 km depth, the approximate depth of unconsolidated sediment. In this case, the rest of the inferred fault parameters are: SAF, 18.5 ± 1.1 mm/yr slip rate and 10.9 ± 1.3 km locking depth; SJF, 18.2 ± 1.7 mm/yr combined CF + CCF slip rate and 11.3 ± 2.9 km locking depth. These parameters are indistinguishable within the uncertainty from the values inferred when surface creep is not included. The effect of creep on the geodetic data is small, and confined to distances within a few kilometers of the fault. We conclude that any bias in the fault slip rate resulting from the neglect of shallow creep is minimal. Finally, note that the creep does not appear to be continuous along the entire fault segment; site VARN, located approximately 300 m west of the fault trace near the north end of the Salton Sea, does not appear to indicate any surface creep, while some InSAR pixels located equally close to the fault show a significant offset. Some of these differences may result from the time-dependent nature of shallow creep.

4. Discussion

[32] Fundamentally, geodetic measurements of strain provide an indirect measure of fault slip rates, which must be inferred through a model. Because modeling assumptions such as material rheology, fault geometry, or variations in material properties are determined prior to the inversion of data, their impact on the result is not reflected in the formal error statistics. To address this question in the case of the southern SAF system, where some previous studies suggested significant disagreements between geodetic and geologic or seismic data [e.g., *Bennett et al*., 2004; *Smith-Konter et al*., 2011], we considered several models with different assumptions regarding elastic properties and the fault geometry to permit a direct comparison of their effects.

[33] The results indicate that incorporation of heterogeneous material properties inferred from the SCEC CVM-H 6.3 tomographic model does not produce a significant asymmetry in the strain rates, and does not significantly affect the inferred slip rates and locking depths in the southern SAF system. Therefore, neglect of elastic heterogeneity is not a likely source of disagreement between previously reported results. This is not surprising, given that the tomographic model shows a modest rigidity contrast of a factor of ~1.3 across the deep part of the SAF; *Fay and Humphreys* [2005] and *Fialko* [2006] have shown that a much stronger and more vertically coherent shear modulus contrast would be required to produce a measurable effect on the geodetic data.

[34] *Schmalzle et al*. [2006] pointed out an asymmetry in the surface velocity field across the Carrizo segment of the SAF, and interpreted it in terms of a relatively strong (up to a factor of 2) contrast in the shear modulus of the upper crust. Contrasts in the effective viscosity of the ductile substrate have also been proposed as a possible cause of asymmetric surface strain rates; for example, *Malservisi et al*. [2001] argued that the effects of laterally variable viscosity help explain geodetic observations in the eastern California shear zone, although *Vaghri and Hearn* [2012] concluded that plausible viscosity contrasts in the lower crust are unable to produce a strong asymmetry in surface strain rates.

[35] We have demonstrated that minor changes in the assumed location of the steadily slipping "fault root" at the brittle-ductile transition can explain the observed asymmetry in surface strain rates, and furthermore significantly impact the inferred fault slip rates. In our models, allowing the Southern SAF to dip at 60° to the northeast better reproduces the observed strain asymmetry across the fault's surface trace, and decreases its inferred slip rate by as much as 6 mm/yr. The magnitude of this effect is more than three times the formal uncertainty computed in the inversion, even though the position of the dislocation edge moved only 6 km horizontally. This highlights the ease with which an incorrect position for the dislocation edge at depth can introduce a significant bias in the results. Locking depths are also strongly affected by the assumed fault geometry, because they trade off closely with the slip rate on each fault. The depth of seismicity below a fault provides a reasonable estimate for the depth of the brittle-ductile transition [*Nazareth*

and Hauksson, 2004; *Smith-Konter et al*., 2011], therefore good agreement of the geodetically inferred locking depth with the depth of seismicity can also provide an independent check on the inferred slip rates.

[36] In our preferred model, the SAF and SJF slip at roughly equal rates of 18 ± 1 and 19 ± 2 mm/yr, respectively. The SAF rate is in agreement with geologic measurements [*Van der Woerd et al*., 2006; *Behr et al*., 2010], in contrast to results obtained when assuming a vertical fault. Geologic studies indicating a combined slip rate of 10–14 mm/yr on the CCF and CF strands [*Blisniuk et al*., 2010] are somewhat lower than this model suggests. However, if some of the additional deformation we attribute to the dislocations at depth is accommodated in the upper crust on other nearby structures such as the San Felipe Fault, Buck Ridge Fault, or by distributed faulting and block rotation, geodetic and geologic data may not be inconsistent. In fact, *Janecke et al*. [2010] have reported significant distributed deformation near the "blind" CF segment in the San Felipe Hills, contributing to their higher integrated total slip rate of 20 mm/yr across the SJF zone. Finally, the inferred locking depths of 10 ± 1 km and 12 ± 3 km for the SAF and SJF are in good agreement with the depth of seismicity in the region, resolving a previously reported discrepancy between geodetic and seismic locking depth along this section of the SJF [*Smith-Konter et al*., 2011]. These observations suggest that earlier reports of a disagreement between geodetic and geologic slip rates on these faults [*Bennett et al*., 2004] may have been an artifact of sparse geodetic data or incorrect modeling assumptions. In particular, our results suggest that long-term variations in fault slip rates are not required by the data, and that the slip rates on major faults of the southern SAF system may have been roughly constant on time scales of 10^4–10^6 years.

5. Conclusions

[37] We have explored two possible sources of bias in geodetic models of the southern SAF system: heterogeneous properties of the crust and assumptions about fault geometry at depth. The results indicate that elastic heterogeneity as inferred from seismic tomography does not significantly impact the inferred slip rates and locking depths of the major faults, so we conclude that neglecting variations in material properties is not likely to introduce a bias in the results. This conclusion should generally hold for regions with moderate variations in material properties.

[38] In the second case, we have shown that even small changes in the assumed position of a fault at depth can produce a significant effect on the inferred model parameters. In particular, the introduction of a dipping SAF as suggested by an observed strain asymmetry [*Fialko*, 2006] along with seismic and other geophysical evidence [*Lin et al*., 2007; *Fuis et al*., 2012] reduces our estimate of the SAF slip rate (and consequently increases the inferred SJF slip rate) by as much as 6 mm/yr. Compared to models with a vertical SAF, the dipping model appears to be in better agreement with all available geophysical and geologic evidence. The introduction of a dislocation below the Clark branch of the SJF does not strongly affect the inferred fault parameters, but results in a better overall fit to the geodetic data without increasing the number of parameters. Together the two proposed changes in geometry explain the observed asymmetric strain rate patterns across the two faults, and future models of the region will benefit from a careful consideration of the dislocation geometry at depth.

[39] **Acknowledgments.** This work was supported by USGS (grant G09AP00025), NASA (grant NNX09AD23G) and SCEC (contribution number 1648). This material is based on data services provided by the UNAVCO Facility with support from the National Science Foundation (NSF) and National Aeronautics and Space Administration (NASA) under NSF Cooperative Agreement EAR-0735156. The inversion program described in the text is available from the authors on request.

References

Barbot, S., Y. Fialko, and D. Sandwell (2009), Three-dimensional models of elasto-static deformation in heterogeneous media, with applications to the Eastern California Shear Zone, *Geophys. J. Int.*, *179*, 500–520, doi:10.1111/j.1365-246X.2009.04194.x.

Becker, T. W., J. L. Hardebeck, and G. Anderson (2005), Constraints on fault slip rates of the southern california plate boundary from gps velocity and stress inversions, *Geophys. J. Int.*, *160*, 634–650, doi:10.1111/j.1365-246X.2004.02528.x.

Behr, W. M., et al. (2010), Uncertainties in slip-rate estimates for the Mission Creek strand of the southern San Andreas fault at Biskra Palms Oasis, southern California, *Geol. Soc. Am. Bull.*, *122*, 1360–1377, doi:10.1130/B30020.1.

Bennett, R. A., W. Rodi, and R. E. Reilinger (1996), Global positioning system constraints on fault slip rates in southern California and northern Baja, Mexico, *J. Geophys. Res.*, *101*, 21,943–21,960, doi:10.1029/96JB02488.

Bennett, R. A., A. M. Friedrich, and K. P. Furlong (2004), Codependent histories of the San Andreas and San Jacinto fault zones from inversion of fault displacement rates, *Geology*, *32*, 961–964, doi:10.1130/G20806.1.

Blisniuk, K., T. Rockwell, L. A. Owen, M. Oskin, C. Lippincott, M. W. Caffee, and J. Dortch (2010), Late Quaternary slip rate gradient defined using high-resolution topography and ^{10}Be dating of offset landforms on the southern San Jacinto Fault zone, California, *J. Geophys. Res.*, *115*, B08401, doi:10.1029/2009JB006346.

Cleary, M. P. (1978), Elastic and dynamic response regimes of fluid-impregnated solids with diverse microstructures, *Int. J. Solids Struct.*, *14*, 795–819, doi:10.1016/0020-7683(78)90072-0.

Fay, N., and G. Humphreys (2005), Fault slip rates, effects of elastic heterogeneity on geodetic data, and the strength of the lower crust in the Salton Trough region, southern California, *J. Geophys. Res.*, *110*, B09401, doi:10.1029/2004JB003548.

Fialko, Y. (2004), Probing the mechanical properties of seismically active crust with space geodesy: Study of the co-seismic deformation due to the 1992 M_w 7.3 Landers (southern California) earthquake, *J. Geophys. Res.*, *109*, B03307, doi:10.1029/2003JB002756.

Fialko, Y. (2006), Interseismic strain accumulation and the earthquake potential on the southern San Andreas fault system, *Nature*, *441*, 968–971, doi:10.1038/nature04797.

Fialko, Y., Y. Khazan, and M. Simons (2001), Deformation due to a pressurized horizontal circular crack in an elastic half-space, with applications to volcano geodesy, *Geophys. J. Int.*, *146*, 181–190, doi:10.1046/j.1365-246X.2001.00452.x.

Fuis, G. S., D. S. Scheirer, V. E. Langenheim, and M. D. Kohler (2012), A new perspective on the geometry of the san andreas fault in southern california and its relationship to lithospheric structure, *Bull. Seismol. Soc. Am.*, *102*, 236–251, doi:10.1785/0120110041.

Janecke, S. U., et al. (2010), High geologic slip rates since early Pleistocene initiation of the San Jacinto and San Felipe Fault zones in the San Andreas Fault system, Southern California, USA, *Geol. Soc. Am. Spec. Pap.*, *475*, 1–48, doi:10.1130/2010.2475.

Johnson, H. O., D. C. Agnew, and F. K. Wyatt (1994), Present-day crustal deformation in southern California, *J. Geophys. Res.*, *99*, 23,951–23,974, doi:10.1029/94JB01902.

Kendrick, K. J., D. M. Morton, S. G. Wells, and R. W. Simpson (2002), Spatial and temporal deformation along the northern San Jacinto fault, southern California: Implications for slip rates, *Bull. Seismol. Soc. Am.*, *92*, 2782–2802, doi:10.1785/0120000615.

Lin, G., P. M. Shearer, and E. Hauksson (2007), Applying a three-dimensional velocity model, waveform cross correlation, and cluster analysis to locate southern California seismicity from 1981 to 2005, *J. Geophys. Res.*, *112*, B12309, doi:10.1029/2007JB004986.

Loveless, J. P., and B. J. Meade (2011), Stress modulation on the san andreas fault by interseismic fault system interactions, *Geology*, *39*(11), 1035–1038, doi:10.1130/G32215.1.

Lovely, P., J. H. Shaw, Q. Liu, and J. Tromp (2006), A structural vp model of the salton trough, california, and its implications for seismic hazard, *Bull. Seismol. Soc. Am.*, *96*(5), 1882–1896, doi:10.1785/0120050166.

Lundgren, P. E., A. Hetland, Z. Liu, and E. J. Fielding (2009), Southern San Andreas–San Jacinto fault system slip rates estimated from earthquake cycle models constrained by GPS and interferometric synthetic aperture radar observations, *J. Geophys. Res.*, *114*, B02403, doi:10.1029/2008JB005996.

MacKay, D. J. C. (2003), Information Theory, Inference, and Learning Algorithms, Cambridge Univ. Press, Cambridge, UK.

Malservisi, R., K. P. Furlong, and T. H. Dixon (2001), Influence of the earthquake cycle and lithospheric rheology on the dynamics of the eastern california shear zone, *Geophys. Res. Lett.*, *28*(14), 2731–2734, doi:10.1029/2001GL013311.

Manzo, M., Y. Fialko, F. Casu, A. Pepe, and R. Lanari (2011), A quantitative assessment of DInSAR measurements of interseismic deformation: the Southern San Andreas Fault case study, *Pure Appl. Geophys.*, doi:10.1007/s00024-011-0403-2.

Meade, B. J., and B. H. Hager (2005), Block models of crustal motion in southern California constrained by GPS measurements, *J. Geophys. Res.*, *110*, B03403, doi:10.1029/2004JB003209.

Nazareth, J. J., and E. Hauksson (2004), The seismogenic thickness of the southern california crust, *Bull. Seismol. Soc. Am.*, *94*, 940–960, doi:10.1785/0120020129.

Neal, R. M. (2003), Slice sampling, *Ann. Stat.*, *31*, 705–767, doi:10.1214/aos/1056562461.

Nur, A., and J. Mavko (1974), Postseismic viscoelastic rebound, *Science*, *183*, 204–206, doi:10.1126/science.183.4121.204.

O'Connell, R. J., and B. Budiansky (1974), Seismic velocities in dry and saturated cracked solids, *J. Geophys. Res.*, *79*, 5412–5426, doi:10.1029/JB079i035p05412.

Petersen, M. D., and S. G. Wesnousky (1994), Fault slip rates and earthquake histories for active faults in Southern California, *Bull. Seismol. Soc. Am.*, *84*, 1608–1649.

Platt, J. P., and T. W. Becker (2010), Where is the real transform boundary in California?, *Geochem. Geophys. Geosyst.*, *11*, doi:10.1029/2010GC003060.

Plesch, A., C. Tape, J. Shaw, and members of the USR working group (2009), CVM-H 6.0: Inversion integration, the San Joaquin Valley and other advances in the community velocity model, *Proc. Ann. SCEC Meeting*, *19*, 260–261.

Rockwell, T., C. Loughman, and P. Merifield (1990), Late quaternary rate of slip along the San-Jacinto fault zone near Anza, Southern California, *J. Geophys. Res.*, *95*, 8593–8605, doi:10.1029/JB095iB06p08593.

Rymer, M. (2000), Triggered surface slips in the Coachella Valley area associated with the 1992 Joshua Tree and Landers, California, earthquakes, *Bull. Seismol. Soc. Am.*, *90*, 832–848, doi:10.1785/0119980130.

Rymer, M. J., J. Boatwright, L. C. Seekins, J. D. Yule, and J. Liu (2002), Triggered surface slips in the Salton Trough associated with the 1999 Hector Mine, California, Earthquake, *Bull. Seismol. Soc. Am.*, *92*, 1300–1317, doi:10.1785/0120000935.

Savage, J. (1998), Displacement field for an edge dislocation in a layered half-space, *J. Geophys. Res.*, *103*, 2439–2446, doi:10.1029/97JB02562.

Savage, J., and R. Burford (1973), Geodetic determination of relative plate motion in central California, *J. Geophys. Res.*, *78*, 832–845, doi:10.1029/JB078i005p00832.

Savage, J. C. (1990), Equivalent strike-slip earthquake cycles in half-space and lithosphere-asthenosphere earth models, *J. Geophys. Res.*, *95*, 4873–4879, doi:10.1029/JB095iB04p04873.

Savage, J. C., and W. H. Prescott (1978), Asthenosphere readjustment and the earthquake cycle, *J. Geophys. Res.*, *83*, 3369–3376, doi:10.1029/JB083iB07p03369.

Schmalzle, G., T. Dixon, R. Malservisi, and R. Govers (2006), Strain accumulation across the Carrizo segment of the San Andreas Fault, California: Impact of laterally varying crustal properties, *J. Geophys. Res.*, *111*, B05403, doi:10.1029/2005JB003843.

Segall, P. (2010), Earthquake and Volcano Deformation, 432 pp., Princeton Univ. Press, Princeton, NJ.

Sharp, R. V. (1967), San Jacinto fault zone in the Peninsular Ranges of southern California, *Geol. Soc. Am. Bull.*, *78*, 705–730, doi:10.1130/0016-7606(1967)78[705:SJFZIT]2.0.CO;2.

Shen, Z. K., R. W. King, D. C. Agnew, M. Wang, T. A. Herring, D. Dong, and P. Fang (2011), A unified analysis of crustal motion in southern california, 1970–2004: The scec crustal motion map, *J. Geophys. Res.*, *116*(B11), 1–19, doi:10.1029/2011JB008549.

Sieh, K., and P. Williams (1990), Behavior of the southernmost San Andreas fault during the past 300 years, *J. Geophys. Res.*, *95*, 6629–6645, doi:10.1029/JB095iB05p06629.

Smith-Konter, B. R., D. T. Sandwell, and P. Shearer (2011), Locking depths estimated from geodesy and seismology along the san andreas fault system: Implications for seismic moment release, *J. Geophys. Res.*, *116*(B6), 1–12, doi:10.1029/2010JB008117.

Spinler, J. C., R. A. Bennett, M. L. Anderson, S. F. McGill, S. Hreinsdottir, and A. McCallister (2010), Present-day strain accumulation and slip rates associated with southern San Andreas and eastern California shear zone faults, *J. Geophys. Res.*, *100*, B11407, doi:10.1029/2010JB007424.

Suess, P., and J. Shaw (2003), P-wave seismic velocity structure derived from sonic logs and industry reflection data in the los angeles basin, california, *J. Geophys. Res.*, *108*(B3), 2170, doi:10.1029/2001JB001628.

Takeuchi, C., and Y. Fialko (2012), Dynamic models of interseismic deformation and stress transfer from plate motion to continental transform faults, *J. Geophys. Res.*, *117*, B05403, doi:10.1029/2011JB009056.

Vaghri, A., and E. H. Hearn (2012), Can lateral viscosity contrasts explain asymmetric interseismic deformation around strike-slip faults?, *Bull. Seismol. Soc. Am.*, *102*(2), 490–503, doi:10.1785/0120100347.

Van der Woerd, J., Y. Klinger, K. Sieh, P. Tapponnier, F. Ryerson, and A. Meriaux (2006), Long-term slip rate of the southern San Andreas Fault from ^{10}Be–^{26}Al surface exposure dating of an offset alluvial fan, *J. Geophys. Res.*, *111*, B04407, doi:10.1029/2004JB003559.

Wei, M., D. Sandwell, and Y. Fialko (2009), A silent M4.8 slip event of October 3–6, 2006, on the Superstition Hills fault, Southern California, *J. Geophys. Res.*, *114*, B07402, doi:10.1029/2008JB006135.

Wei, M., D. Sandwell, and B. Smith-Konter (2010), Optimal combination of InSAR and GPS for measuring interseismic crustal deformation, *Adv. Space Res.*, *46*, 236–249, doi:10.1016/j.asr.2010.03.013.

Wei, M., D. Sandwell, Y. Fialko, and R. Bilham (2011), Slip on faults in the Imperial Valley triggered by the 4 April 2010 Mw 7.2 El Mayor-Cucapah earthquake revealed by InSAR, *Geophys. Res. Lett.*, *38*, L01308, doi:10.1029/2010GL045235.